Evaluation of y(UTC(NICT)) with respect to NICT-Sr1 for the period MJD 61279 to 61309

We have evaluated the fractional frequency deviation of the time scale UTC(NICT) for the period from MJD 61279 to 61309 (August 27 – September 26 of 2026) to be $\overline{\boldsymbol{y}(\mathbf{UTC}(\mathbf{NICT}))} = \mathbf{+0.73} \times \mathbf{10^{-16}}$, using secondary frequency standard NICT-Sr1.

NICT-Sr1 measured the mean frequency deviation of hydrogen maser $\mathrm{HM}_{1402014}$ to be $\overline{y(\mathrm{HM}_{1402014})} = -1.49797 \times 10^{-13}$, and the frequency of UTC(NICT) was then determined by the Japan Standard Time system.

The optical lattice clock acquired data for 75 297 s (2.9% of the total evaluation period) over four operating intervals on MJD 61284, 61291, 61299, and 61307 as shown in Fig. 3. The resulting uncertainties are represented in the following table according to Circular T notation:

Period of Estimation (MJD)	$\overline{y(\mathrm{UTC(NICT)}}$	u_{A}	u_{B}	$u_{\mathrm{A/Lab}}$	$u_{\mathrm{B/Lab}}$	u_{Srep}	uptime
61279 – 61309	+0.73	0.26	0.70	1.59	0.57	1.7	2.9%

Effect	Uncertainty					
$u_{\mathrm{A/Sr}}$	0.26	✓				
$u_{\mathrm{B/Sr}}$	0.70		✓			
HM: linear trend estimation	1.18			✓		
HM: stochastic noise	1.06			✓		
Optical-microwave comparison / microwave transfer	0.20				✓	
Sequenced laser pulling	0.54				✓	
Uncertainty of Sr as SRS	1.7					✓

Table 1. Results of evaluation. All numbers are in parts of 10^{-16}.

The evaluation employs the recommended value of the ^{87}Sr clock transition as a secondary representation of the second: $\nu(^{87}\mathrm{Sr})$ = 429 228 004 229 872.992 Hz with its relative standard uncertainty of $u_{\mathrm{Srep}} = 1.7 \times 10^{-16}$, approved by the CCTF in September 2025, and applied from March 27, 2026.

u_{A} is the Type A uncertainty of NICT-Sr1 as an optical standard. It represents the statistical uncertainty determined by interleaved measurements [1] and improves as $u_{\mathrm{A/Sr}} = 7 \times 10^{-15}/\sqrt{\tau}$ with measurement time.

u_{B} is the Type B uncertainty of NICT-Sr1 [1 – 3] summarized in section 9, extended to include the uncertainty of the gravitational redshift.

$u_{\mathrm{A/Lab}}$ and $u_{\mathrm{B/Lab}}$ represent the uncertainty of the link of NICT-Sr1 to UTC(NICT), consisting of

- Type A uncertainty $u_{\mathrm{A/Lab}} = 1.59 \times 10^{-16}$, which represents the linear trend estimation of the HM ($u_{\mathrm{l/trend}}$) and the uncertainty due to the stochastic noise of the HM during unobserved intervals ($u_{\mathrm{l/stoch}}$).
- Type B uncertainty $u_{\mathrm{B/Lab}} = 5.7 \times 10^{-17}$ due to the frequency comparison between the clock's optical signal and the microwave signals of NICT's time scale. In addition to the frequency comb conversions and distribution of the microwave signals, we include an additional systematic uncertainty $u_{\mathrm{seq}} = 5.4 \times 10^{-17}$ due to electrically induced frequency pulling of the clock laser synchronous with the interrogation sequence.

1. Modifications of NICT-Sr1 since previous publications

The details of NICT-Sr1 are described in [1, 2]. The optical-to-rf conversion and connection to the hydrogen maser flywheel is discussed in [3], and its integration with the Japan Standard Time System in [4]. Since the publication of these reports, the phase reference of the clock laser was changed in November 2024 to exclude clock-cycle synchronous Doppler shifts. A source of such shifts may be stress or vibration induced in the clock structure by switching of the magnetic trapping coils.

Before the modification, the reflective reference surface used in the clock laser phase stabilization was mounted to the optical table, separate from the science chamber. Following the modification, the direction of the clock laser has been reversed to pass through the end mirror of the optical lattice, where an added optical element now provides the reflective reference surface. By attaching the reference surface to the lattice end mirror, the phase of the clock laser remains fixed relative to the lattice antinodes that locate the trapped atoms. This modification does not change the presented uncertainty budget.

2. Gravitational redshift re-evaluation

To expand our understanding of geodetic effects on the operation of optical clocks, NICT is collaborating with the Geospatial Information Authority of Japan (GSI). This collaboration enables NICT-Sr1 to operate with a gravitational red shift correction uncertainty of less than 10^{-17} [5]. It recently provided a revised gravity potential value of 62 636 101.92±0.30 m^2/s^2 at the position of the trapped atoms [6], corresponding to a gravitational red shift of $8.361(3) \times 10^{-15}$.

We acknowledge the support of K. Matsuo, Y. Hiraoka, B. Miyahara, E. Harima, S. Fukaya, and M. Nakashima at GSI in addition to R. Ichikawa at NICT. A publication with additional details is expected soon.

The revised red shift correction is reflected in the uncertainty budget of section 9.

3. Sequenced clock laser pulling

We have located a source of error in our measurements of the steered clock laser frequency which results from electrically induced frequency pulling synchronous with the clock operating sequence. The existence of this shift is evident in a change of the measured HM frequency by several 10^{-15} when the clock's sequencer system is directly connected to the clock laser system by a shared frequency reference signal. Its nature is revealed by measuring the ground level voltage of the connecting cable relative to that of the clock laser system, as shown in Figure 1.

We find that in the original configuration of the sequencer system, the observed voltage between the ground potentials corresponds directly to its digital output state. During the interrogation of the clock's atomic sample, the voltage differs by 3.11(2) mV from the mean value over the full cycle. We consider the potential difference a source of bias in the sensitive Pound-Drever-Hall lock of the laser to its reference cavity. When this results in frequency pulling synchronous with the sequencer output, the momentary frequency that samples the atomic transition differs from the continuous full-cycle mean recorded by the frequency comb measurement. This creates an error in the link between the atomic reference and the HM participating in international time, and we assign a corresponding uncertainty u_{seq} as part of $u_{\mathrm{B/Lab}}$.

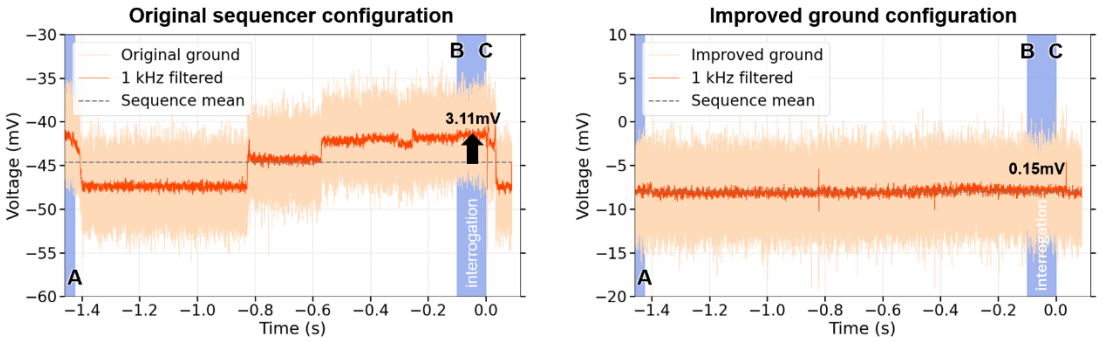

Fig. 1. Electrical measurements: Sampled voltages on the ground signal of a coaxial cable connected to the clock's sequencer and control systems, measured relative to the ground level of the laser system. *(Left)* With the original electrical configuration of the clock sequencer, the voltage visibly and repeatably varies with the sequencer's output state. The voltage measured during the interrogation of the atomic sample (B-C) differs by 3.11 mV from the mean value over the full cycle (A-C). Where such a voltage biases the locking to the reference cavity, the continuous frequency measurement by an optical frequency comb differs from the momentary frequency that the atoms are exposed to. *(Right)* Improved grounding of the sequencer system reduces both the overall ground potential difference and its variation with the output state. The voltage measured during interrogation (B-C) now differs by only 0.15 mV from the full-cycle mean (A-C).

Modifications to the grounding configuration of the cavity lock have reduced the sensitivity to this sequenced pulling effect but did not eliminate it entirely. We take two additional steps to mitigate and characterize it, illustrated in fig. 2:

First, we electrically isolate all connections between the clock control system and the laser system, using opto-isolators and RF transformers. This reduces the measured frequency error from $\delta y_{\mathrm{max}} = 19.1(3.8) \times 10^{-16}$ to $-6.9(3.0) \times 10^{-16}$, an attenuation by $a_{\mathrm{iso}} = -0.36(17)$.

With this result supporting the observed ground level difference and variation as the source of the measurement error, the second step is improved grounding of the clock sequencer to local Earth. For the measurement shown in fig. 1, this reduces the voltage difference between the full-cycle mean and the momentary value during atomic interrogation from 3.11(2) mV to 0.15(3) mV, an attenuation by $a'_{\mathrm{GND}} = 0.048(8)$. To account for scatter between repeated measurements, we adopt a more conservative value of $a_{\mathrm{GND}} = 0.066(22)$. Clock measurements confirm this attenuation to the limit of the measurement resolution, detecting a reduction of the measured frequency error from $19.1(3.8) \times 10^{-16}$ to $-1.4(2.6) \times 10^{-16}$. Performing these measurements without electrical isolation between the clock and laser systems helps resolve the attenuation despite the noise of the HM that serves as flywheel in measurements that require manual reconfiguration.

With both mitigations in place, we expect a residual frequency error $\delta y_{\mathrm{res}} = a_{\mathrm{iso}}\, a_{\mathrm{gnd}}\, \delta y_{\mathrm{max}} = -4.6 \times 10^{-17}$ with uncertainty $u_{\mathrm{res}} = 2.8 \times 10^{-17}$. This configuration serves as a reference point with an error that is close to negligible when compared to the statistical uncertainties of the characterizing measurements. Figure 2 summarizes the frequency differences measured between different electrical configurations.

NICT-Sr1 also operates with electrically isolated clock laser system and improved grounding of the sequencer system (i.e. with both mitigations in place) in all measurements used for the TAI calibration. We assign the systematic uncertainty $u_{\mathrm{seq}} = \sqrt{\delta y_{\mathrm{res}}^2 + u_{\mathrm{res}}^2} = 5.4 \times 10^{-17}$ to cover the magnitude of this frequency error and its uncertainty. Previously reported measurements may have underestimated $u_{\mathrm{B/Lab}}$ by more than this amount, although none of them include the specific electrical connection resulting in the highly visible error δy_{max}.

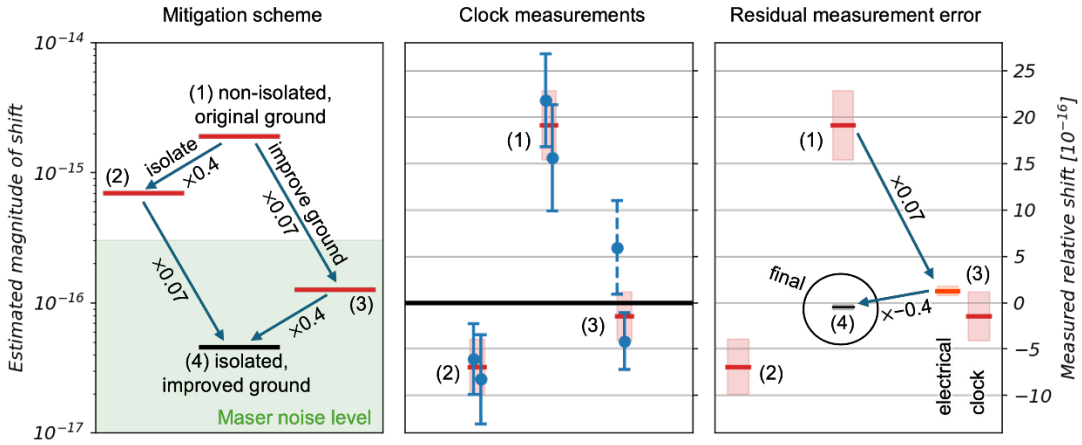

Fig. 2. Evaluation and mitigation of measurement error from sequenced laser pulling.
(Left) By investigating the effect of isolating the electrical systems (1⇨2) and the effect of the improved grounding of the sequencer system (1⇨3) separately, we obtain an estimate of the residual error for the TAI calibration measurements performed with both mitigations in place (4).
(Center) The same condition (4) is used as reference for evaluating the measurement errors by clock measurements of the frequency shifts in conditions (1), (2) and (3). Error bars show the individual differences observed through consecutive comparisons of the clock to the flywheel HM. Shaded areas represent a combined 1σ confidence interval for the estimated frequency shift of (1) to (3). For the attenuated shift of condition (3), we include a measurement performed in a preliminary grounding arrangement (dashed), the solid error bar shows a measurement of condition (3) using the finalized grounding arrangement used throughout the TAI calibration.
(Right) The evaluation of the final attenuated measurement error $\delta y_{\mathrm{res}} = -4.6(2.8) \times 10^{-17}$ yields the gray confidence band of (4). It is determined by combining the measured shift δy_{max} of (1) with the two attenuation factors. Clock measurements of (2) determine $a_{\mathrm{iso}} \approx -0.4$, but we find $a_{\mathrm{GND}} \approx 0.07$ from the electrical measurements shown in fig. 1. The 'electrical' confidence interval illustrates $a_{\mathrm{GND}}\ \delta y_{\mathrm{max}}$ for comparison with the 'clock' measurements of the center figure. Here the noise of the flywheel HM reference makes it challenging to resolve the small residual shift in condition (3), but the results appear consistent with the 'electrical' result to statistical limitations.

4. Evaluation of the frequency of hydrogen maser $HM_{1402014}$ with respect to NICT-Sr1 over 30 days

We transfer the behavior of the reference HM to an Er:fiber comb by stabilizing a heterodyne beat between the 82nd harmonic of the frequency comb's approximately 100 MHz repetition rate and an 8.2 GHz signal from a dielectric resonator oscillator (DRO) phase-locked to the 100 MHz signal of $HM_{1402014}$.

In the operation of NICT-Sr1, ^{87}Sr atoms are laser-cooled using a two-stage laser cooling technique and loaded to a vertically oriented one-dimensional optical lattice. The stabilization of the clock laser to the atomic transition creates an optical frequency reference at 698 nm. A transfer laser at 1397 nm is phase-locked to the 698 nm signal using the frequency-doubled component generated by a PPLN waveguide. The residual infrared component generates a beat signal with the frequency comb. This beat is counted both directly and through a tracking oscillator to allow rejection of cycle slips. Zero-deadtime counters record stabilized and unstabilized beat signals to identify and remove data segments affected by cycle slips or miscounts.

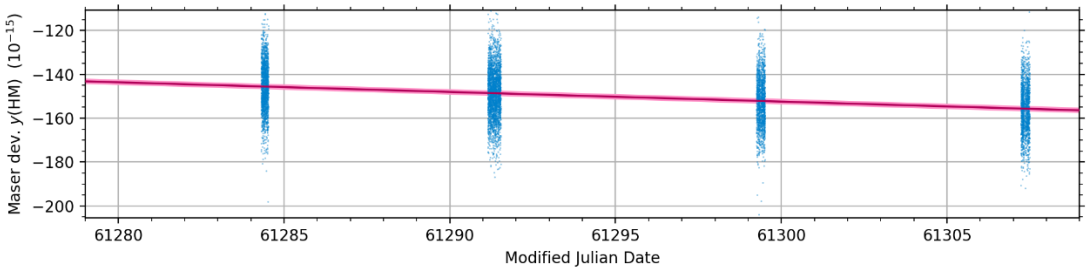

Fig. 3. Distribution of maser frequency measurements in terms of fractional deviation y(HM) from the nominal frequency. The solid line indicates the linear fit used to obtain the mean value over the evaluation interval.

After this confirmation, the fractional deviation of the HM frequency from its nominal value is stored as a pre-averaged value for a series of 10 s bins. Weights are assigned according to the number of contributing data points in each bin.

5. Statistical uncertainty of the HM frequency measurement

We determine a statistical uncertainty of the maser frequency measurement $u_{\mathrm{stat}} = 1.18 \times 10^{-16}$ from the residuals of a linear fit by extrapolating the Allan deviation from the region limited by white frequency noise (30–7 200 s) to the full length of available data.

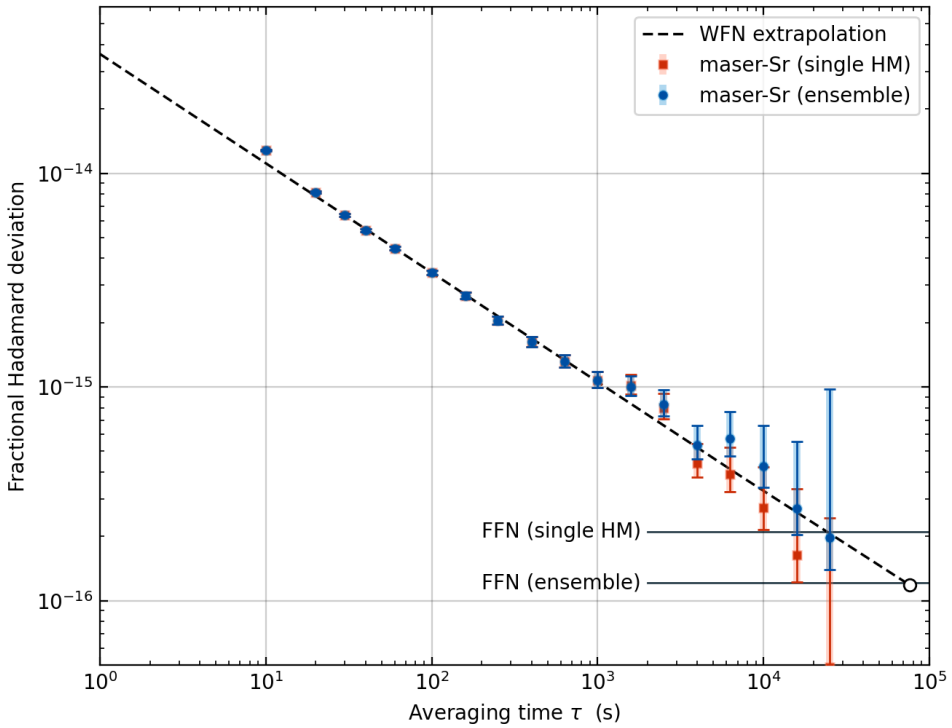

Fig. 4. Instability of maser frequency measurements with respect to NICT-Sr1. Circles highlighted in blue and squares highlighted in red show the overlapping Hadamard deviation for the residuals from a linear fit with and without correction for deviation of the HM from linear drift, as determined by using an ensemble of 3 HMs. Gaps have been removed by contracting the drift-removed data into a continuous interval. Error bars indicate 1σ uncertainties, calculated for white frequency noise. The black dashed line indicates the extrapolation to the full length of available data, used to obtain the statistical uncertainty u_{stat} indicated by the open mark, which contributes to the determined u_l. For long averaging times, the Hadamard deviation is expected to fall to a level consistent with the maser stability model, indicated by the upper horizontal line indicating the flicker frequency noise (FFN) level for a single maser, and by the lower line for the ensemble, where the instability is improved by a factor of $1/\sqrt{N_{\mathrm{ens}}}$.

When plotting the instability of the frequency measurements for $HM_{1402014}$ in terms of the Hadamard deviation, we expect a floor $\sigma_L^2 \approx a_{-1}$ due to flicker frequency noise (FFN), and ultimately a growing instability modeled as flicker-walk frequency modulation (FWFM). We treat these components as part of the intrinsic HM frequency evolution that is to be measured, rather than the measurement noise. The following section considers their effect on the unobserved periods of the HM behavior.

There is a difference of −17 949 s between the midpoint (MJD 61294.0) of the evaluation period and the barycenter of the data (approximately MJD 61294.21). The estimation of the maser drift over this time interval introduces an uncertainty of $u_{\mathrm{drift}} = 3 \times 10^{-18}$, such that

$$u_{\mathrm{l/trend}} = \left(u_{\mathrm{stat}}^2 + u_{\mathrm{drift}}^2\right)^{1/2} = 1.18 \times 10^{-16} .$$

6. Treatment of stochastic noise during unobserved intervals

For intermittent clock operation, phase and frequency excursions of the HM during unobserved intervals contribute significant measurement uncertainty [2, 8].

To mitigate their effect, we include a total of three HMs in the evaluation ($HM_{1402004}$, $HM_{1402014}$ and $HM_{1402015}$). Their relative phase is continuously monitored by the Japan Standard Time dual-mixer time-difference (DMTD) system [9]. We calculate the frequency difference of each HM from the ensemble average and check for abnormal behavior during the evaluation period. We then determine the frequency of $HM_{1402014}$ with respect to the ensemble. By subtracting frequency offset and linear trend from this relative frequency, we obtain residuals that approximate the instantaneous deviation of $HM_{1402014}$ from a pure linear drift, while summing to zero over the evaluation period. We use these residuals (calculated for a set of one-hour intervals) to correct the HM frequency measured with respect to the Sr clock (Fig. 5). The result is an improved representation of the mean frequency and linear drift of $HM_{1402014}$ over the complete evaluation period. A weighted linear fit is applied to the corrected data to find the frequency corresponding to the midpoint of the 30-day interval. The ensemble-based corrections result in a change of the reported HM frequency by $+7 \times 10^{-18}$ compared to the result obtained using only $HM_{1402014}$.

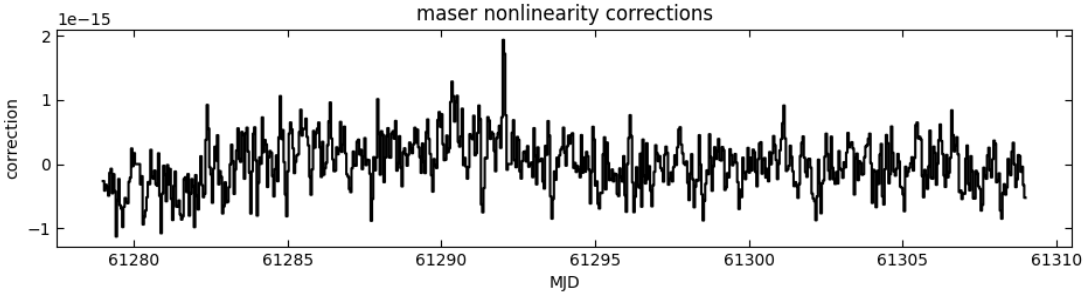

Fig.5. Corrections applied to the assumed frequency of $HM_{1402014}$ based on its difference from the ensemble mean. As a correction for instantaneous HM frequency excursions, the overall mean is set to be zero.

We characterize the typical instability of a single maser based on evaluation of several years of continuous data using three-corner-hat methods and find that for large averaging times it is well-described by an Hadamard variance $\sigma_H^2(\tau) = a_{-1} + a_{-3}\tau^2$. Here, $a_{-1} = (2.1 \times 10^{-16})^2$ represents FFN [10] while the slow-varying noise that dominates the long-term instability through $a_{-3} = (1.9 \times 10^{-22}/\mathrm{s})^2$ is typically referred to as FWFM [11]. We follow the approach described in the supplement of ref. [12] to determine the uncertainty of extrapolating from arbitrarily distributed data to the full evaluation period. This yields a distribution-specific sensitivity to the HM's noise

power spectral density (PSD) [12], which we obtain from the observed maser instabilities a_{-1} and a_{-3} through the relations

$$\text{FFN:} \quad \sigma_{\mathrm{H}}^2(\tau) = \frac{1}{2}\ln\left(\frac{256}{27}\right) h_{-1} \quad \text{for } S_y^{\mathrm{FFN}} = h_{-1}\, f^{-1} \quad \text{and} \tag{1}$$

$$\text{FWFM:} \quad \sigma_{\mathrm{H}}^2(\tau) = \frac{16}{6}\pi \ln\left(\frac{3}{4}\cdot 3^{11/16}\right) h_{-3}\, \tau^2 \quad \text{for } S_y^{\mathrm{FWFM}} = h_{-3}\, f^{-3} \quad , \tag{2}$$

according to refs. [11, 13]. Additional information on the procedure is available in ref. [8]. Despite the complexity of FFN and FWFM in the temporal domain, the noise can always be expressed as a sum over normally distributed sources, and there is no correlation between the noise encountered in separate masers. The maser ensemble therefore shows the same uncertainty reduction with $N_{\mathrm{ens}}^{-1/2}$ as other noise types.

For the present measurement distribution and PSDs, this leads to the uncertainty contributions $u_{\mathrm{l/FFN}} = 1.03 \times 10^{-16}$ and $u_{\mathrm{l/FWFM}} = 2.60 \times 10^{-16}$, which we include as $u_{\mathrm{l/stoch}} = 1.06 \times 10^{-16}$. Since the frequency evaluation for each TAI calibration is performed separately and based on non-overlapping data sets, the uncertainty $u_{\mathrm{l/stoch}}$ represents errors that are uncorrelated between calibrations.

7. Systematic uncertainty for the link of UTC(NICT) to NICT-Sr1

In addition to the sequenced frequency pulling described in section 3, our intermittent measurements of the maser frequency are easily affected by phase shifts resulting from diurnal temperature variations as well as thermalization effects at the start of operation. Frequency combs and measurement instruments are operated continuously to avoid start-up effects and to maintain a constant heat load in the laboratory. This contribution to the evaluation of the systematic lab-side link uncertainty is described in ref. [3]. The value reported here is calculated as

$u_{\mathrm{B/Lab}}^2 = u_{\mathrm{seq}}^2 + u_{\mathrm{DMTD}}^2 + u_{\mathrm{dist}}^2 + u_{\mathrm{comb}}^2 + u_{\Delta\mathrm{HM}}^2 = (5.7 \times 10^{-17})^2$:

$u_{\mathrm{seq}} = 5.4 \times 10^{-17}$ is the residual uncertainty due to the sequenced laser frequency pulling.

$u_{\mathrm{DMTD}} = 3.1 \times 10^{-18}$ is the largest expected continuous error of the DMTD measurement of a HM frequency relative to UTC(NICT).

$u_{\mathrm{dist}} = 1.3 \times 10^{-17}$ is the uncertainty due to diurnal delay variation in the signal distribution, modeled as a sinusoidal with amplitude $a_{\mathrm{dist}} = 0.18\,\mathrm{ps}$. For short daily operating times we consider the maximum derivative $\delta y_{\max} = 2\pi\, a_{\mathrm{dist}}/1\mathrm{d} = 1.3 \times 10^{-17}$. For extended operation, the maximum frequency error is limited by the worst-case, peak-to-peak timing change of $2\, a_{\mathrm{dist}}$, such that $\delta y_{\max} = 2\, a_{\mathrm{dist}}/T_{\mathrm{op}}$, a stricter limit when $T_{\mathrm{op}} > 86\,400\,\mathrm{s}/\pi \approx 27500\,\mathrm{s}$. The listed value is an average over all days of operation in this reported period.

$u_{\mathrm{comb}} = 4.1 \times 10^{-18}$ accounts for persistent errors in the optical-to-rf conversion, determined by comparing two independent frequency comb systems.

$u_{\Delta\mathrm{HM}} = 1.4 \times 10^{-17}$ is the uncertainty due to diurnal variation in the measurements of the DMTD system, modeled as a sinusoidal with amplitude $a_{\mathrm{DMTD}} = 0.19\,\mathrm{ps}$. While diurnal effects cancel out in the 30-day comparison of HM and UTC(NICT), they affect the evaluation through the HM ensemble correction calculated for shorter intervals. The listed value is an average over all days of operation in this reported period.

8. Frequency deviation of UTC(NICT)

The frequency difference between $HM_{1402014}$ and UTC(NICT) over the evaluation period is typically calculated as

$$y(\mathrm{UTC(NICT)} - \mathrm{HM}_{1402014}) = (\delta_b - \delta_a)/T, \quad (3)$$

where δ_a and δ_b represent the time difference UTC(NICT) − $HM_{1402014}$ at the beginning and end of an evaluation interval of length T. These values are continuously measured by the DMTD system [9] and reported to BIPM, where they are used in the EAL generation and made available at https://webtai.bipm.org/ftp/pub/tai/data/. A comparison to the independent TIC data is used to inspect the data for measurement errors. We find

$$y(\mathrm{UTC(NICT)} - \mathrm{HM}_{1402014}) = +1498.694 \times 10^{-16},$$

which is used to calculate $\overline{y(\mathrm{UTC(NICT)})}$ from $\overline{y(\mathrm{HM}_{1402014})}$.

9. Accuracy of NICT-Sr1

The uncertainty $u_{\mathrm{B/Sr}}$ consists of systematic effects acting on the atomic transition frequency, its interrogation, and comparison to international time. Except for the revised gravitational redshift evaluation described in section 2, the corrections and uncertainties remain unchanged from earlier evaluations of NICT-Sr1 [1,2,7] and are summarized below:

Effect	Correction (10^{-17})	Uncertainty (10^{-17})
Blackbody radiation	517.7	3.8
Lattice scalar / tensor	0	5.3
Lattice hyperpolarizability	–0.2	0.1
Lattice E2/M1	0	0.5
Probe light	0.04	0.03
DC Stark	0.1	0.2
Quadratic Zeeman	50.7	0.3
Density	0.2	0.1
Background gas collisions	0	1.8
Line pulling	0	0.1
Servo error	-0.1	1.7
Total	568.5	7.0
Gravitational redshift	–836.1	0.3
Total (with gravitational effect)	–267.6	7.0

Table 2. Systematic corrections and their uncertainties for NICT-Sr1.

10. References

[1] H. Hachisu and T. Ido, "Intermittent optical frequency measurements to reduce the dead time uncertainty of frequency link," Jpn. J. Appl. Phys. **54**, 112401 (2015).

[2] H. Hachisu, G. Petit, F. Nakagawa, Y. Hanado and T. Ido, "SI-traceable measurement of an optical frequency at low 10^{-16} level without a local primary standard," Opt. Express **25**, 8511 (2017).

[3] N. Nemitz *et al.*, "Hydrogen maser flywheels for optical clocks," J. Phys.: Conf. Ser. **2889,** 012019 (2024).

[4] H. Hachisu *et al.,* "Contributions of the optical lattice clock NICT-Sr1 to TAI calibration and UTC (NICT) steering," J. Phys.: Conf. Ser. **2889,** 012018 (2024).

[5] R. Ichikawa *et al.,* "Geodetic Measurements and Quantitative Evaluation for Reduced Gravitational Redshift Uncertainty of NICT Optical Frequency Standards," in Proc. IEEE IFCS-EFTF 2023, Toyama, Japan, available at https://www.eftf.org/previous-meetings

[6] R. Ichikawa *et al.,* "Recent Geodetic Efforts at NICT for Stable Operation of Optical Atomic Clocks and High-Precision Chronometric Levelling," submitted for presentation at the 2026 Annual Meeting of the Japan Geoscience Union (JpGU) held jointly with the American Geophysical Union (AGU), May 2026, Chiba, Japan.

[7] H. Hachisu, F. Nakagawa, Y. Hanado and T. Ido, "Months-long real-time generation of a time scale based on an optical clock," Sci. Reports **8**, 4243 (2018).

[8] N. Nemitz *et al*., "Absolute frequency of ^{87}Sr at 1.8×10^{-16} uncertainty by reference to remote primary frequency standards," Metrologia **58**, 025006 (2021)

[9] F. Nakagawa *et al.*, "Development of multichannel dual-mixer time difference system to generate UTC(NICT)," IEEE Trans. Instrum. Meas. **54,** 829 (2005).

[10] D. Allan, "Time and frequency (time-domain) characterization, estimation, and prediction of precision clock and oscillators," IEEE UFFC **34**, 647 (1987).

[11] W. J. Riley, "Handbook of Frequency Stability Analysis," NIST Special Publication 1065 (2008)

[12] C. Grebing *et al.*, "Realization of a timescale with an accurate optical lattice clock," Optica **3**, 563-569 (2016).

[13] S. T. Dawkins, J. J. McFerran and A. Luiten, "Considerations on the Measurement of the Stability of Oscillators with Frequency Counters," IEEE Trans. UFFC **54**, 918-925 (2007).